Facile synthesis of sulfur-doped mesoporous carbon nitride supported defect-rich cobalt sulfide for electrocatalytic water oxidation

Devesh Kumar Singh, Vellaichamy Ganesan*, Dharmendra Kumar Yadav, and Mamta Yadav

Department of Chemistry, Institute of Science, Banaras Hindu University

Varanasi-221 005, UP, India

Telephone: + +91-542-2307321; Fax: + 91-542-2368127

E-mail: velganesh@yahoo.com and velgan@bhu.ac.in
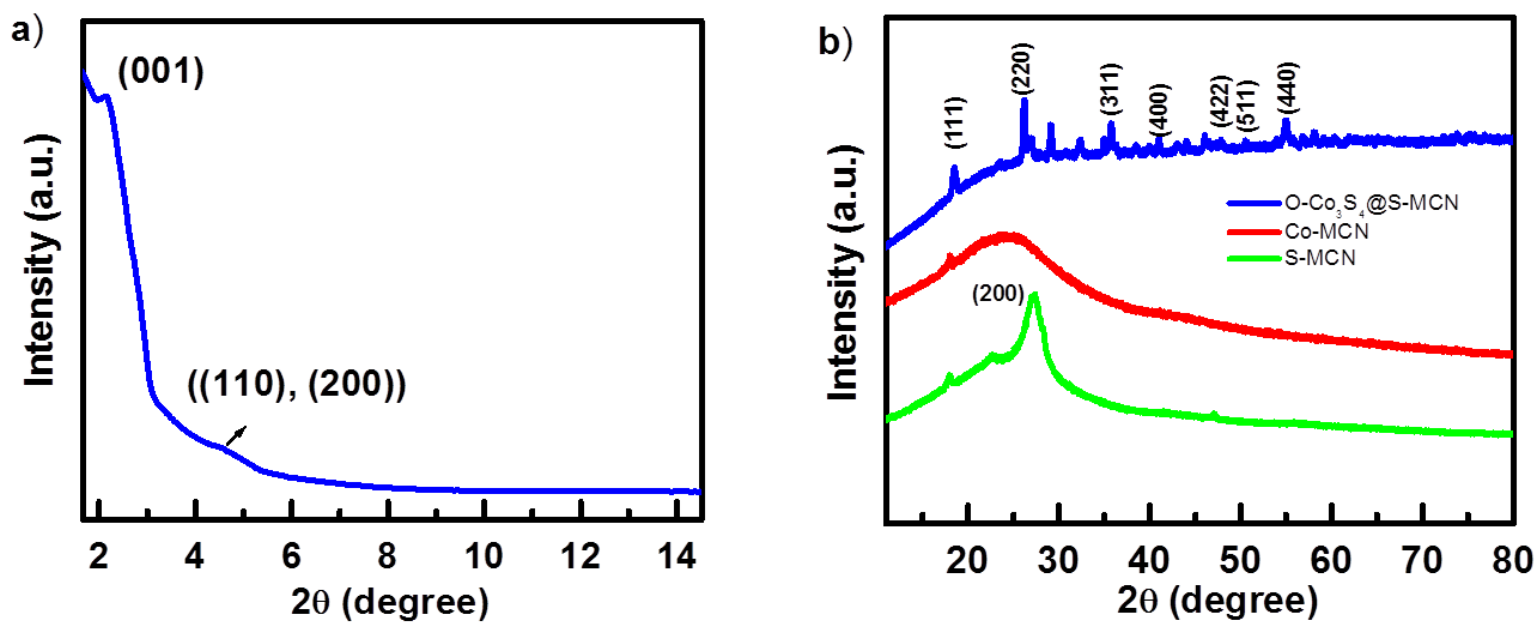

* Corresponding author

Figure S1. Low-angle powder XRD pattern of O-Co$_3$S$_4$@S-MCN material (a) and wide-angle Powder XRD patterns O-Co$_3$S$_4$@S-MCN, Co-MCN, and S-MCN materials (b).

FT-IR spectra of O-Co_3S_4@S-MCN, Co-MCN, and S-MCN are shown in Figure S2. A broad

peak around 3300 cm^{-1} is observed in all three materials (O-Co_3S_4@S-MCN, Co-MCN, and S-

MCN) which can be corroborated to the N-H stretching vibrations. Peaks observed around 1620

cm^{-1} represents C=N stretching vibrations. Broadening of this peak in Co-MCN and O-

Co_3S_4@S-MCN materials is observed which is due to the coordination of nitrogen with cobalt.[S1]

For O-Co_3S_4@S-MCN and S-MCN the peak around 1090 cm^{-1} is attributed to the stretching

vibrations of C=S.[S2-S4] Thus, the presence of sulfur in the framework of MCN is strongly

supported by the presence of C=S stretching vibrations in case of O-Co_3S_4@S-MCN and S-MCN

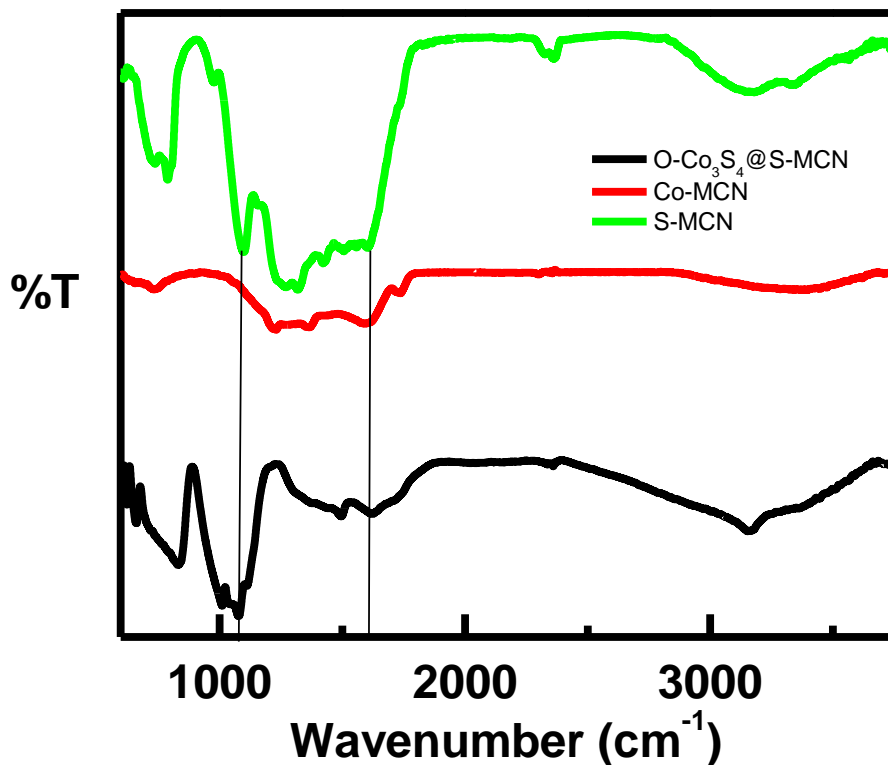materials. No such band is observed in the Co-MCN material.

Figure S2.   FT-IR spectra of Co_3S_4@S-MCN, Co-MCN, and S-MCN materials.
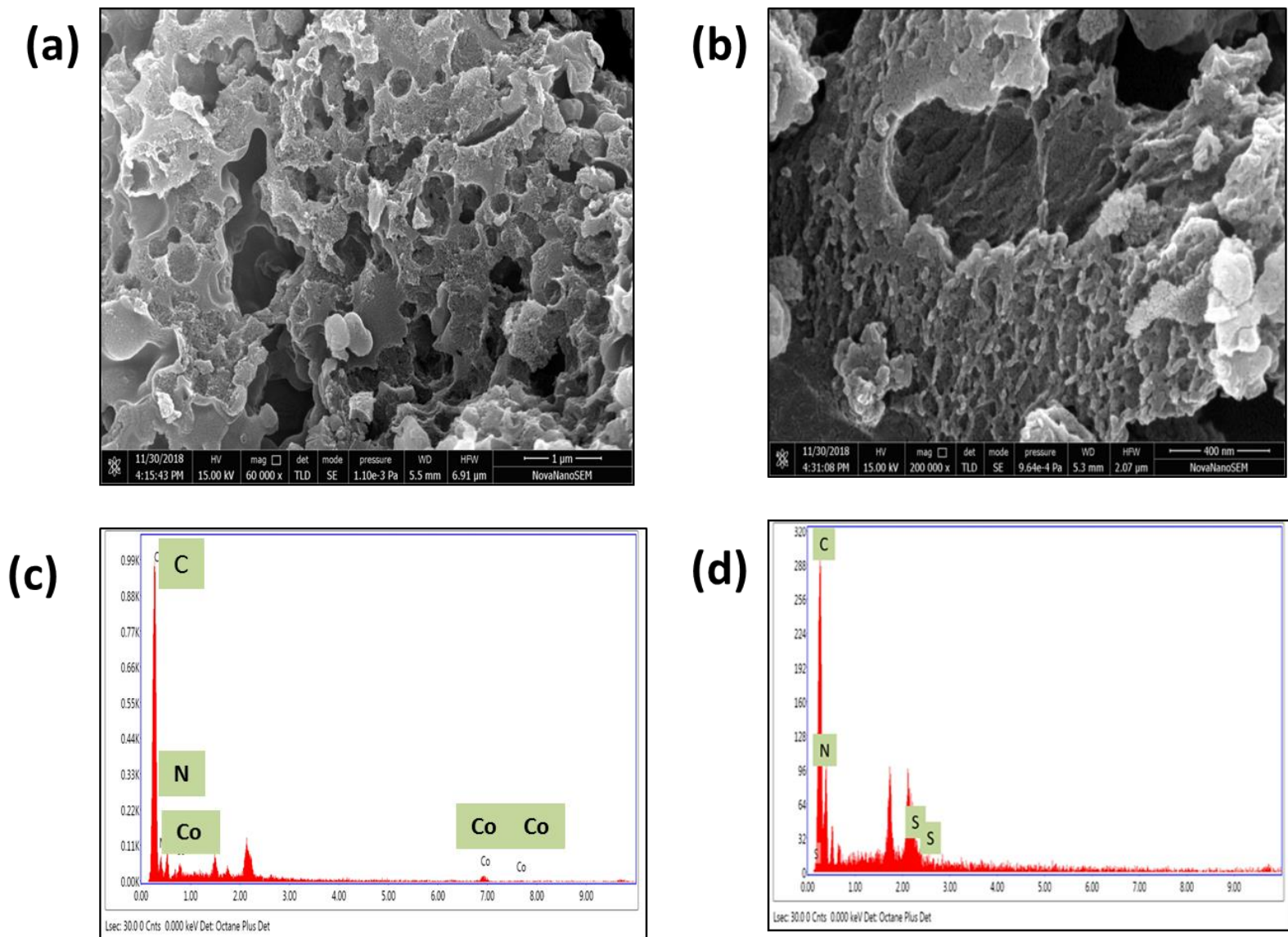
Figure S3. SEM images (a and b) and EDAX spectra (c and d) of Co-MCN (a and c), and S-MCN (b and d) materials.
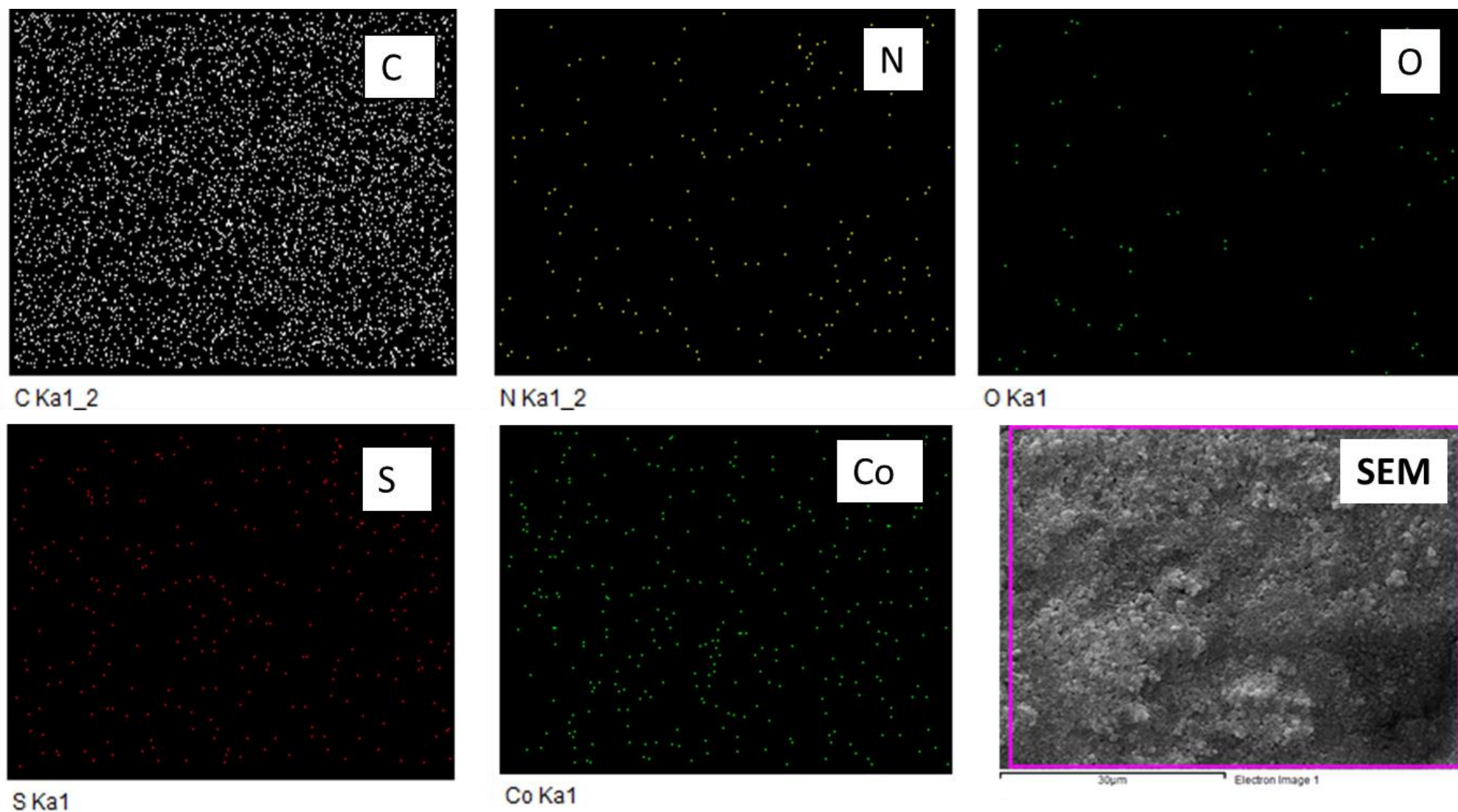
Figure S4(a). Elemental mapping images of O-Co$_3$S$_4$@S-MCN together with the corresponding SEM image.
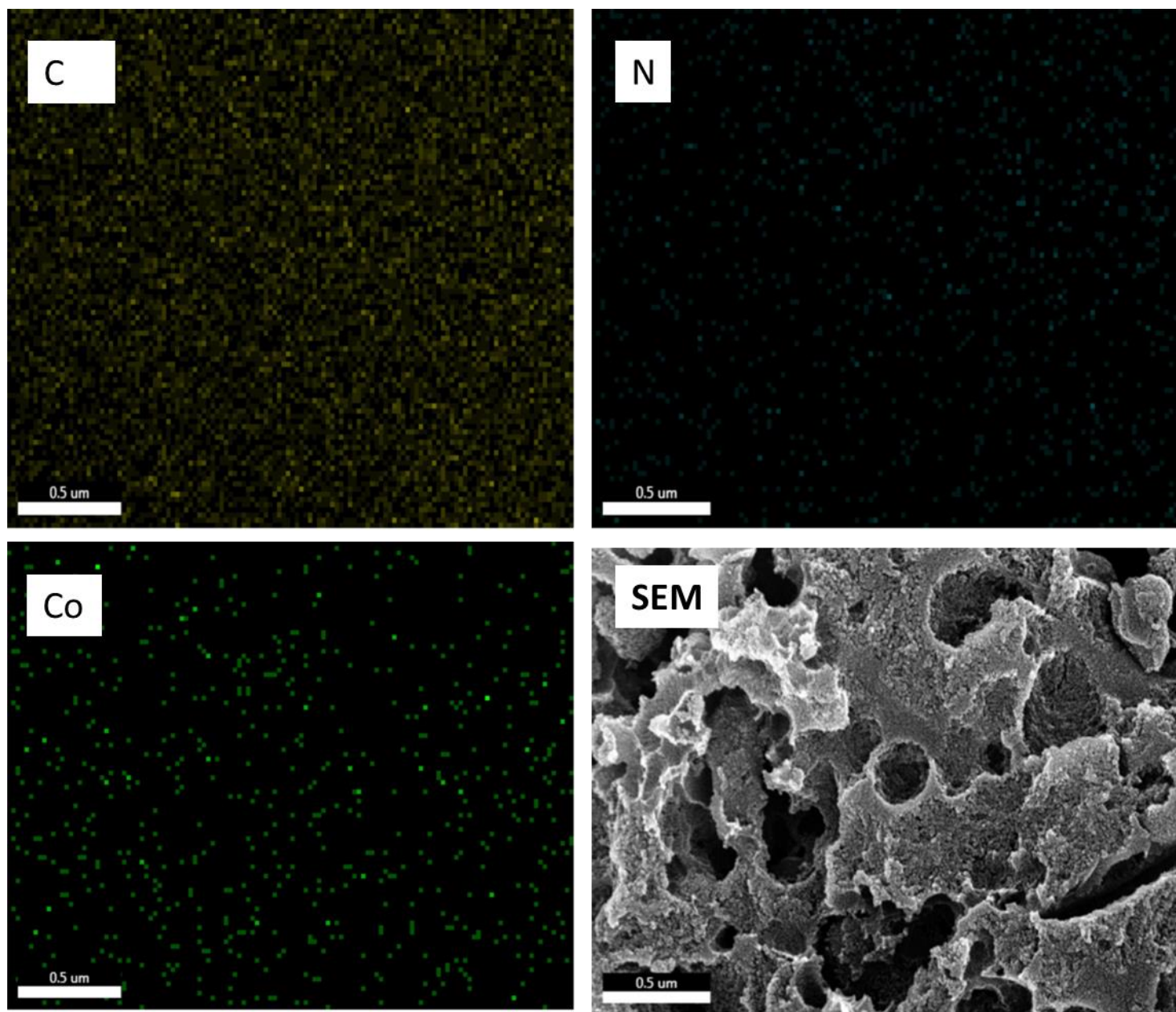
Figure S4(b). Elemental mapping images of Co-MCN together with the corresponding SEM image.
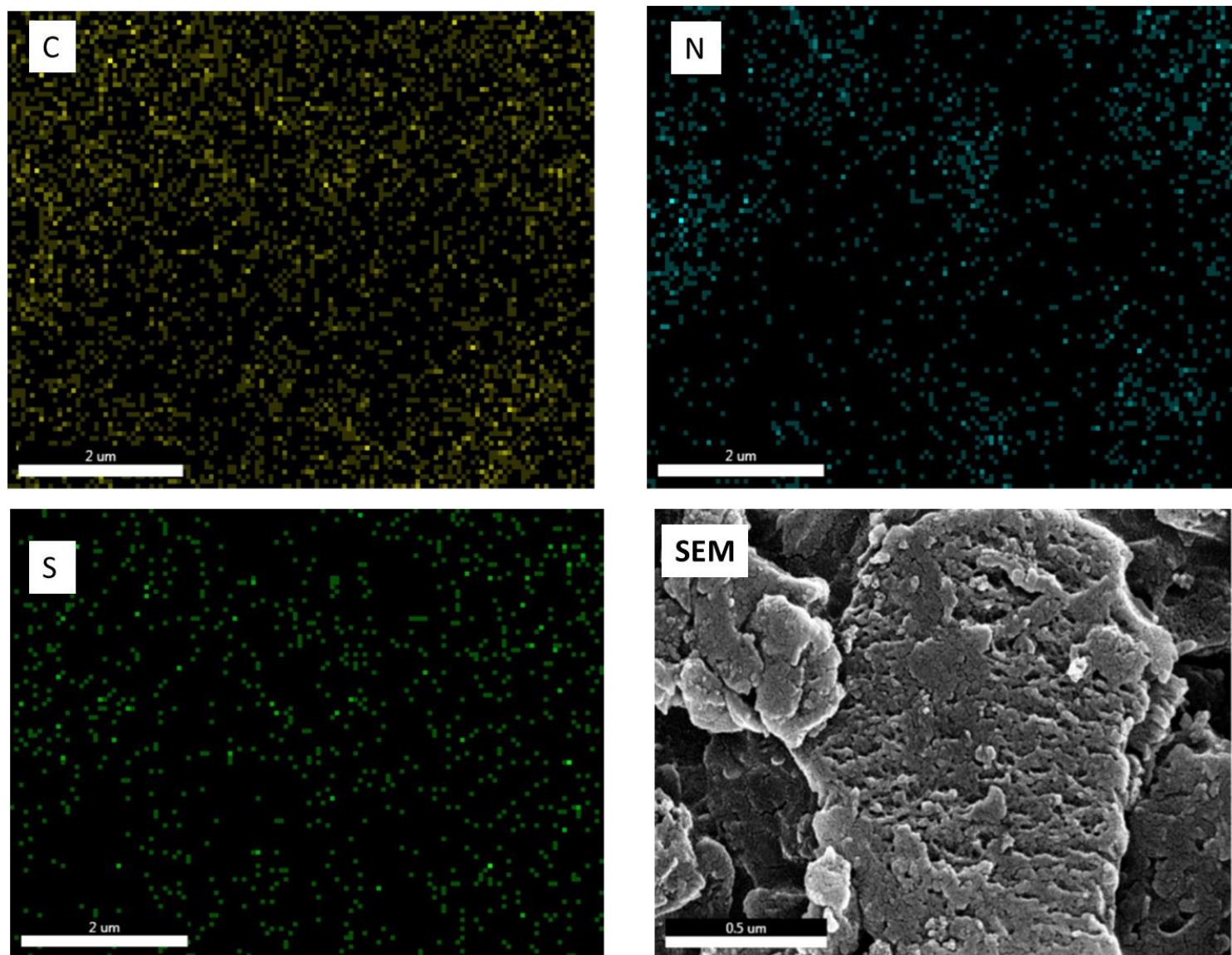
Figure S4(c). Elemental mapping images of S-MCN together with the corresponding SEM
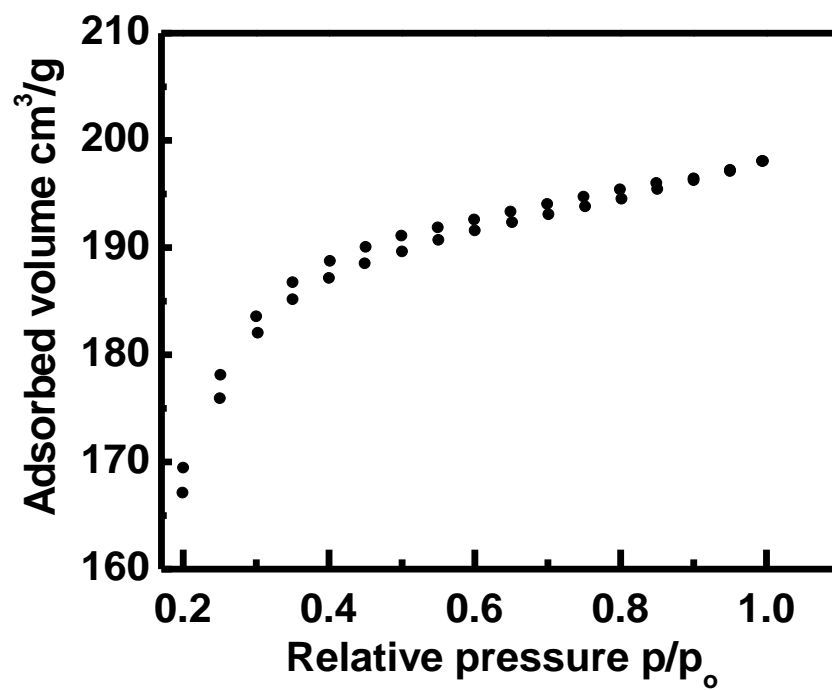
image.

Figure S5. Nitrogen adsorption desorption isotherm of O-Co$_3$S$_4$@S-MCN.

Determination of open circuit potential (OCP)

Two electrode system was used for the OCP determination. Modified GCs were used as working electrodes in 1.0 M KOH. Variation of potential with time was recorded using the OCP technique available in the software (660C electrochemical workstation, CH Instruments, USA). All materials were found to achieve a constant potential within 400 s. The constant potential value in each case is considered as OCP for the respective electrode. The obtained variation is shown in Figure S6. OCP values are 0.83, 0.93, and 0.0.89 V, respectively for GC/O-Co_3S_4@S-MCN, GC/Co-MCN and GC/S-MCN
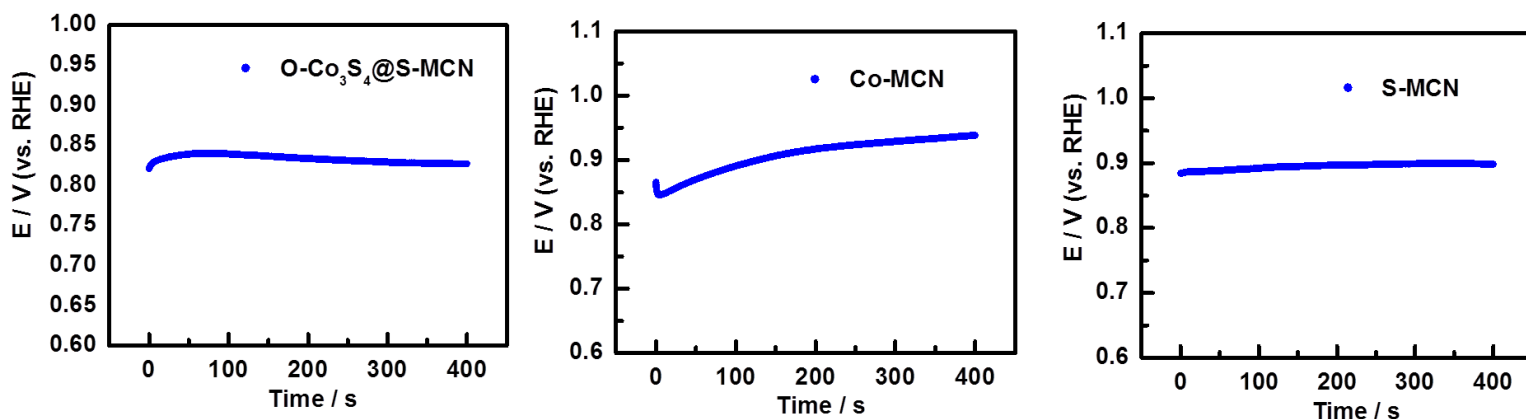

Figure S6. Potential variation with time for OCP determination of GC/O-Co_3S_4@S-MCN, GC/ Co-MCN, and GC/S-MCN in 1.0 M KOH.
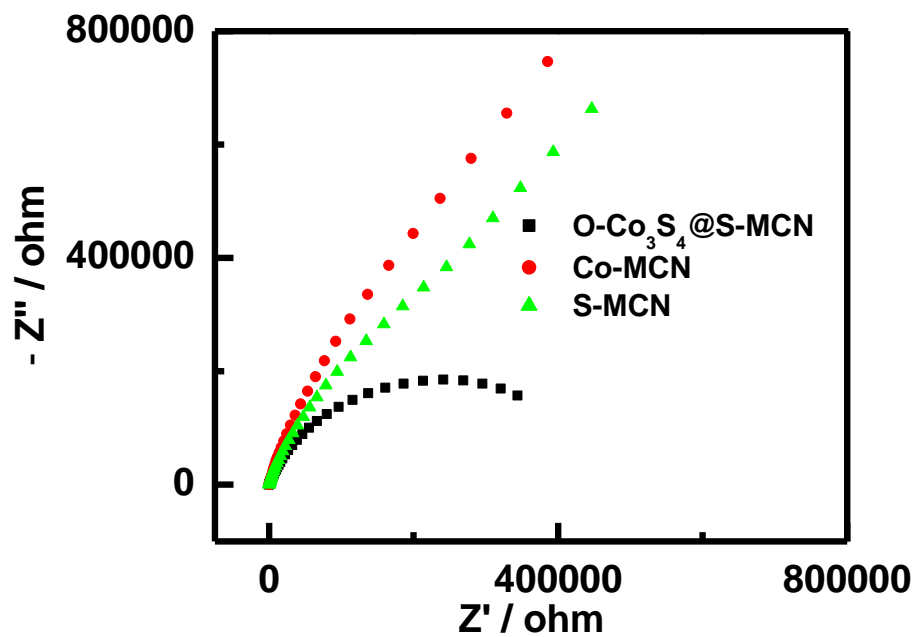
Figure S7. Nyquist plot of GC/O-Co$_3$S$_4$@S-MCN, GC/Co-MCN, and GC/S-MCN recorded in aqueous 1.0 M KOH solution at their respective open circuit potential. Frequency range: 1 MHz to 0.01 Hz and Amplitude: 0.005 V.

Procedure for calculation of electrochemically active surface area (ECSA) and roughness factor

CV responses of GC/O-Co$_3$S$_4$@S-MCN, GC/Co-MCN, GC/S-MCN, and GC/RuO$_2$, were recorded with incremental scan rates from 1.08 to 2.14 V in which no obvious faradic process takes place and only double layer charging occurs (Figure S8(A-D)). The variation in the anodic current density is plotted with the scan rate (Figure S8(A'-D')). The slope obtained from the current density *vs.* scan rate plot gives double layer capacitance (C$_{dl}$). The ECSA is calculated based on the equation S1[S5,S6] using the capacitance of the bare GC electrode as 60 µFcm^{-2} per cm^2 ECSA.[S5,S6] The calculated ESCA values are summarized in Table S1. Roughness factor is defined as the ratio between ECSA and geometrical surface area of the electrode. Since the current density is used for the calculation of ECSA in this work, the roughness factor will have the same value as ECSA without units.

$$ECSA = C_{dl}(observed) / C_{dl}(bare\ GC) \qquad\qquad … (S1)$$

Table S1. ECSA of various material coated GC electrodes in 1.0 M KOH

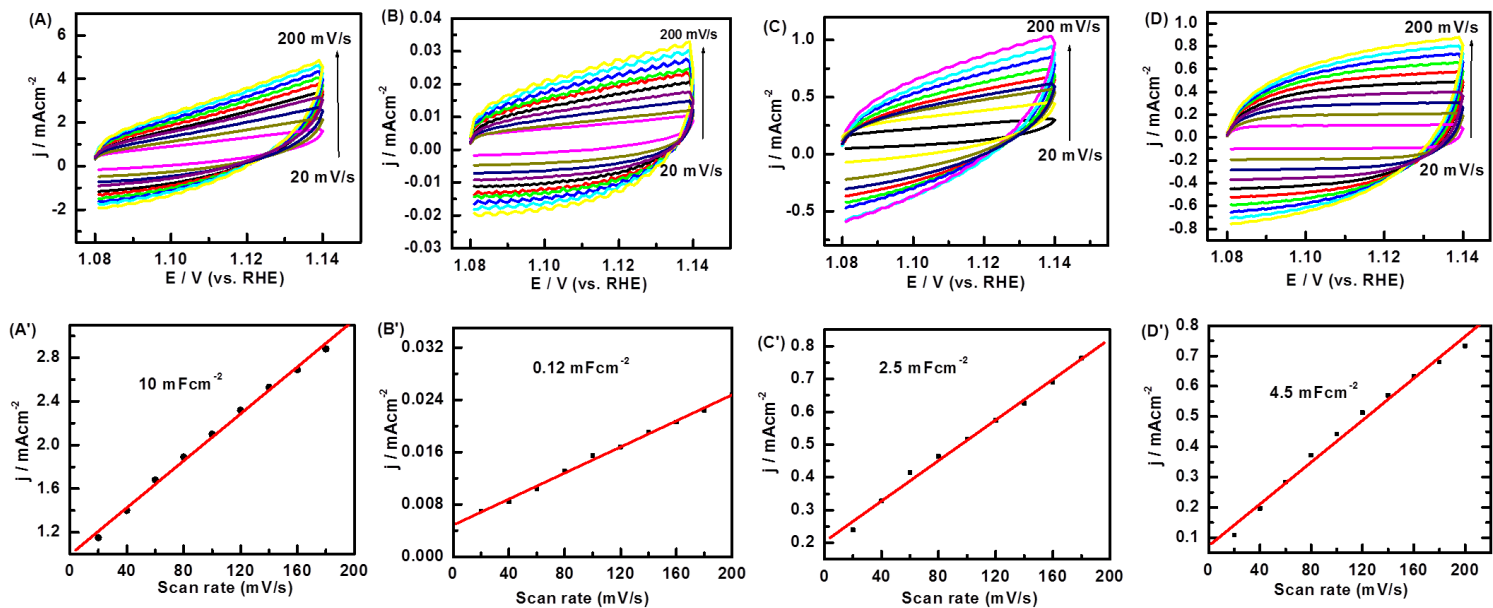| Material	ESCA (cm^2)
O-Co$_3$S$_4$@S-MCN	167
Co-MCN	2
S-MCN	4.3
RuO$_2$	75

Figure S8.   CV responses of O-Co_3S_4@S-MCN (A), Co-MCN (B), S-MCN (C), and RuO_2

(D) in 1.0 M KOH at different scan rates and corresponding variation of current

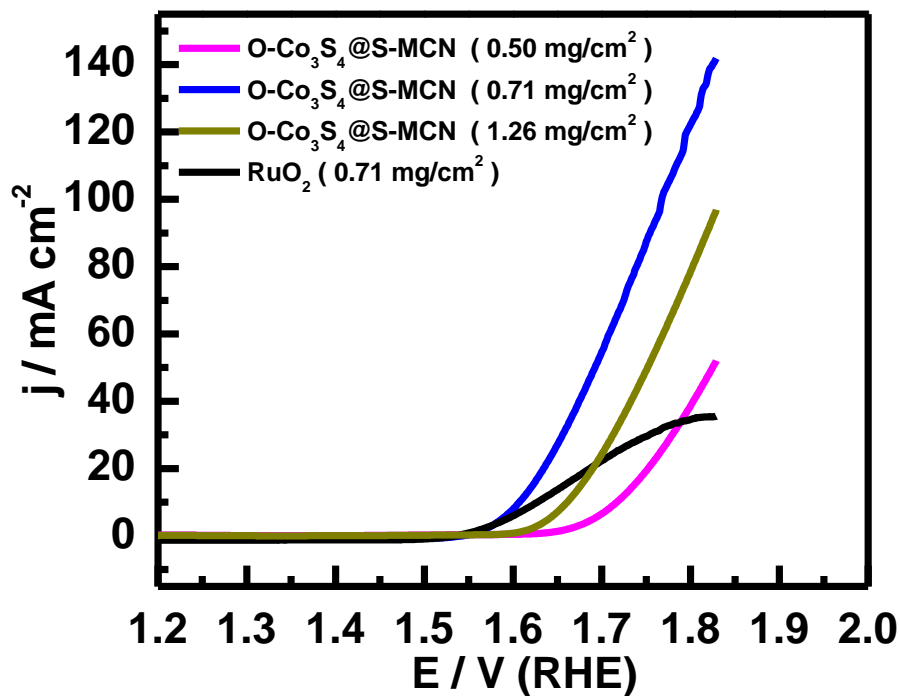density measured at 1.11 V with scan rate (A'- D').

Figure S9. LSV response of GC_{RDE} electrodes modified with different loadings of the O-Co_3S_4@S-MCN or modified with RuO_2 in 1.0 M KOH solution at the rotation rate of 1600 rpm. The values in parenthesis indicate the amount of material coated on the electrode (0.50, 0.71, and 1.26 mg/cm^2 loadings were obtained by coating, 10, 14, and 25 µL of 1% aqueous O-Co_3S_4@S-MCN suspension).

Figure S9 (above) shows the OER response of GC_{RDE} electrodes modified with different loading amounts of the catalyst (O-Co_3S_4@S-MCN) and also with RuO_2 (99.9%) under exactly similar experimental conditions. It is observed that the O-Co_3S_4@S-MCN gives best catalytic response when the loading is kept as 0.71 mg/cm^2 on the electrode.

Figure S10. LSV polarization curves presenting mass activity of O-Co$_3$S$_4$@S-MCN, Co-MCN, S-MCN, and RuO$_2$ materials coated on GC$_{RDE}$ in 1.0 M KOH.

Mass activity (A/g catalyst) of the O-Co$_3$S$_4$@S-MCN, Co-MCN, S-MCN, and RuO$_2$ materials is plotted with the applied potential. On comparing the results at 1.7 V (RHE), O-Co$_3$S$_4$@S-MCN (76 A/g) exhibits 2.5 times higher activity than the RuO$_2$ (31 A/g).

Calculation of turn over frequency (TOF)

The number of active sites on the catalyst was calculated based on the previous reports.[S7-S10] Briefly, CV response was recorded from -0.2 to 0.6 V (*vs.* SCE) in phosphate buffer (pH = 7) at the scan rate of 50 mVs^{-1} (Figure S11). The potential range is chosen in such a way that it should not show any catalytic current in the potential region and it should exhibit only the redox characteristics of the active site. Redox peak observed in CV (Figure S11a) is attributed to the oxidation of cobalt and reduction of the oxidized species in the reverse segment. Assuming that all sites available on the electrode are active, the number of active sites (n) can be calculated from equation S2.[S7-S10]

$$n = Q_{cv} / 2F \qquad \qquad … (S2)$$

where Q_{cv} is the integrated charge calculated from the CV response and F is the Faraday constant (96485 C). From the number of active sites (n), the turn over frequency (TOF) can be calculated using equation S3.[S7-S10]

$$TOF = I / 4nF \qquad \qquad … (S3)$$

where I is the linear sweep voltammetry current. The division by 4 is attributed to the total number of electrons required for the conversion of water to O_2. These results are compared with commercial RuO_2 (Table S2) which clearly indicates the superior performance of the O-Co_3S_4@S-MCN material.

Table S2. Comparison of the TOF measured at different overpotentials for the O-Co_3S_4@S-MCN and RuO_2 materials.

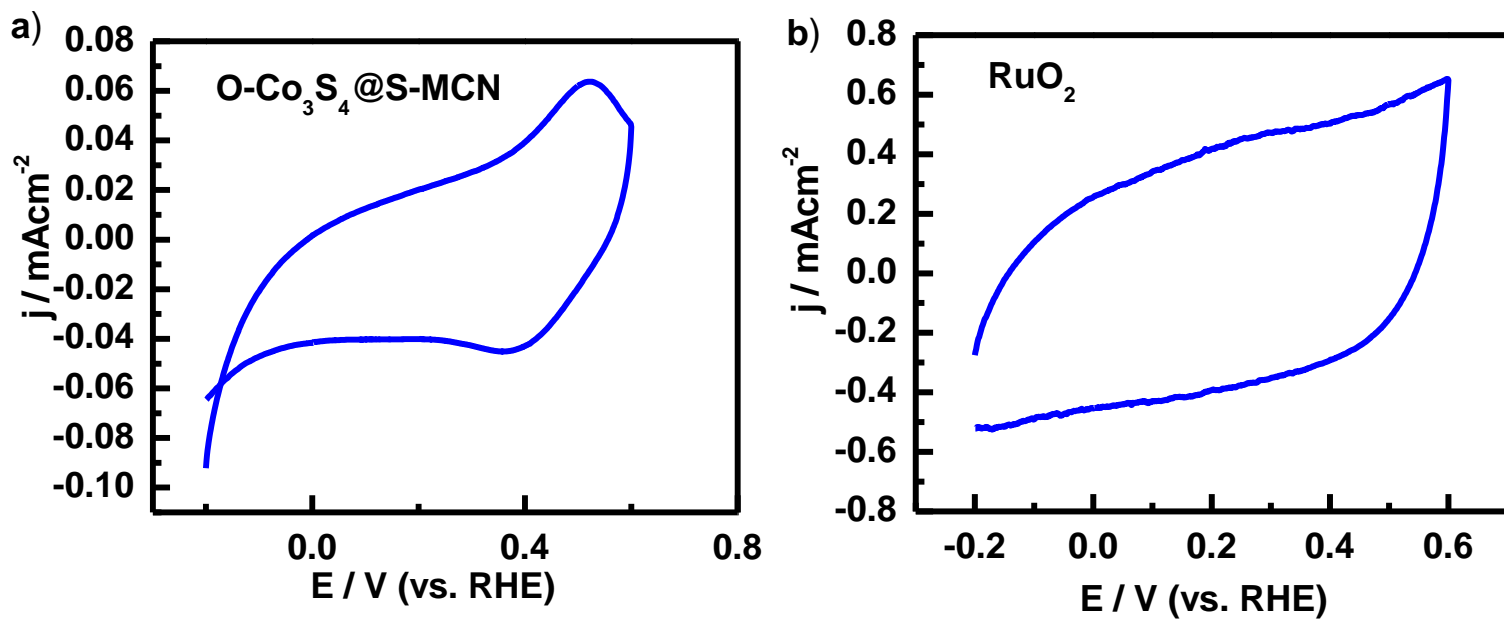| Material	Number of active sites (mole)	Electrolyte	TOF (s^{-1}) at different overpotentials (η)		
			370 mV	400 mV	430 mV
O-Co_3S_4@S-MCN	3.63×10^{-10}	1.0 M KOH	5.0	9.0	14.8
RuO_2	4.04×10^{-9}	1.0 M KOH	0.34	0.5	0.8

Figure S11. CV response of O-Co$_3$S$_4$@S-MCN and RuO$_2$ coated on GC electrodes in 0.1 M phosphate buffer (pH =7).

References

(S1) Aiyappa, H. B.; Thote, J.; Shinde, D. B.; Banerjee, R.; Kurungot, S. Cobalt modified Covalent Organic Framework as a robust water oxidation electrocatalyst. *Chem. Mater*. **2016**, 28, 4375-4379

(S2) Lu, Y-C.; Chen, J.; Wang, A-J.; Bao N.; Feng, J –J.; Wang W.; Shao, L. Facile synthesis of oxygen and sulfur co-doped graphitic carbon nitride fluorescent quantum dots and their application for mercury (II) detection and bio imaging *J. Mater. Chem. C*, **2015**, 3, 73-78.

(S3) Qu, D.; Zheng, M.; Du, P.; Zhou, Y.; Zhang, L.; Li, D.; Tan, H.; Zhao, Z.; Xie, Z.; Sun, Z. Highly luminescent S, N co-doped graphene quantum dots with broad visible absorption bands for visible light photocatalyst. *Nanoscale*, 2013, **5**, 12272-12277.

(S4) You, R.; Dou, H.; Chen, L.; Zheng, S.; Zhang, Y. Graphitic carbon nitride with S and O codoping for enhanced visible light photocatalytic performance. *RSC Adv*. **2017**, 7, 15842–15850.

(S5) Zhang, C.; Shi Y.; Yu, Y.; Du, Y.; Zhang, B. Engineering Sulfur Defects, Atomic Thickness and Porous Structures into Cobalt Sulfide Nanosheets for Efficient Electrocatalytic Alkaline Hydrogen Evolution *ACS Catal.* **2018**, 8, 8077–8083.

(S6) Deng, H.; Zhang, C.; Xie, Y.; Tumlin, T.; Giri, L.; Karnab, S. P.; Lin, J. Laser induced MoS_2/carbon hybrids for hydrogen evolution reaction catalysts. *J. Mater. Chem. A* **2016**, 4, 6824-6830.

(S7) Mohanty, B.; Mahdi, G.-A.; Kretschmer, S.; Ghosh, A.; Guha, P.; Panda S. K.; Jena, B.; Krasheninnikov, A. V.; Jena, B. K. MoS_2 Quantum Dots as an Efficient Catalyst Material for Oxygen Evolution Reaction. *ACS Catal.* **2018**, 8, 1683−1689.

(S8) Merki, D.; Fierro, S.; Vrubel, H.; Hu, X. Amorphous Molybdenum Sulfide Films as Catalysts for Electrochemical Hydrogen Production in Water. *Chem. Sci.* **2011**, *2*, 1262–1267.

(S9) Gao, M.-R.; Cao, X.; Gao, Q.; Xu, Y.-F.; Zheng, Y.-R.; Jiang, J.; Yu, S.-H. Nitrogen-doped graphene supported $CoSe_2$ nanobelt composite catalyst for efficient water oxidation
ACS Nano **2014**, *8*, 3970–3978.

(S10) An, L.; Huang, L.; Zhou, P.; Yin, J.; Liu, H.; Xi, P. A Self-Standing High-Performance Hydrogen Evolution Electrode with Nanostructured $NiCo_2O_4$ /CuS Heterostructures. *Adv. Funct. Mater.* **2015**, 25, 6814–6822.